Infall and outflow motions towards a sample of massive star-forming regions from the RMS survey

N. Cunningham,[1,2,3]⋆ S L. Lumsden,[3] T. J. T. Moore,[4] L T. Maud[5] and I. Mendigutía[3,6]

[1]*Institut de Radioastronomie Millimetrique (IRAM), 300 rue de la Piscine, F-38406 Saint Martin d'Hères, France*
[2]*Green Bank Observatory, 155 Observatory Rd, PO Box 2, Green Bank, WV 24944, USA*
[3]*School of Physics and Astronomy, University of Leeds, Leeds LS2 9JT, UK*
[4]*Astrophysics Research Institute, Liverpool John Moores University, IC2, Liverpool Science Park, 146 Brownlow Hill, Liverpool L3 5RF, UK*
[5]*Leiden Observatory, Leiden University, PO Box 9513, NL-2300 RA Leiden, the Netherlands*
[6]*Centro de Astrobiología, Departamento de Astrofísica (CSIC-INTA), ESA-ESAC Campus, PO Box 78, E-28691 Villanueva de la Cañada, Madrid, Spain*

ABSTRACT

We present the results of an outflow and infall survey towards a distance-limited sample of 31 massive star-forming regions drawn from the Red MSX source (RMS) survey. The presence of young, active outflows is identified from SiO (8–7) emission and the infall dynamics are explored using $HCO^+/H^{13}CO^+$ (4–3) emission. We investigate if the infall and outflow parameters vary with source properties, exploring whether regions hosting potentially young active outflows show similarities or differences with regions harbouring more evolved, possibly momentum-driven, 'fossil' outflows. SiO emission is detected towards approximately 46 per cent of the sources. When considering sources with and without an SiO detection (i.e. potentially active and fossil outflows, respectively), only the ^{12}CO outflow velocity shows a significant difference between samples, indicating SiO is more prevalent towards sources with higher outflow velocities. Furthermore, we find the SiO luminosity increases as a function of the *Herschel* 70 μm to *WISE* 22 μm flux ratio, suggesting the production of SiO is prevalent in younger, more embedded regions. Similarly, we find tentative evidence that sources with an SiO detection have a smaller bolometric luminosity-to-mass ratio, indicating SiO (8–7) emission is associated with potentially younger regions. We do not find a prevalence towards sources displaying signatures of infall in our sample. However, the higher energy HCO^+ transitions may not be the best suited tracer of infall at this spatial resolution in these regions.

Key words: stars: formation – ISM: jets and outflows – ISM: molecules.

1 INTRODUCTION

Infall and outflow motions are an important part of the star-formation process. However, a comprehensive understanding of both processes, particularly towards massive star-forming regions, is still lacking. This is due, in part, to the larger distances and typically more clustered and complex nature of such regions, making it difficult to disentangle the infall and outflow properties of individual objects in a given cluster.

Observationally, young stellar objects (YSOs) of all masses are known to drive bipolar molecular outflows and SiO emission has been effectively used to detect outflows driven by low- ($M_{sun} < 2 M_*$), intermediate- ($2 M_* < M_{sun} < 8 M_*$), and high-mass ($M_{sun} > 8 M_*$) stars (e.g. Gibb et al. 2004; Gibb, Davis & Moore 2007; Duarte-Cabral et al. 2014; Klaassen, Testi & Beuther 2012; Cun-

ningham et al. 2016). The passage of fast shocks is required to disrupt and release SiO from the solid grains into the gas phase (e.g. Schilke et al. 1997; Gusdorf et al. 2008; Guillet, Jones & Pineau Des Forêts 2009; Flower & Pineau des Forêts 2012). Thus, SiO emission, particularly the higher energy transitions, is likely to be an excellent tracer of an active outflow located close to the stellar driving source. Gibb et al. (2004) found SiO emission was preferentially detected towards Class 0 sources in their sample of low-mass stars. Furthermore, those sources with an SiO detection were associated with higher outflow velocities and higher densities, suggesting shock velocity and ambient density are likely to play an important role in the production of SiO in the early stages of low-mass star formation. Bontemps et al. (1996) observed more powerful outflows to be associated with Class 0 sources in their sample of 45 embedded YSOs. Similarly, a decrease of the outflow force with source evolution was observed by Mottram et al. (2017) towards a sample of Class 0 and Class I sources. In the high-mass regime, Gibb et al. (2007) found SiO emission was preferentially

detected towards sources with higher outflow velocities, but were unable to establish the evolutionary nature of individual sources. Further work by Klaassen et al. (2012) found an increase in the integrated intensity of the SiO emission with evolutionary stage, contrary to the observations in the low-mass regime, detecting both infall and outflow signatures towards ultra-compact H II (UCH II) regions. As CO is more readily excited in the ambient medium, it has been suggested (e.g. Bally et al. 1999; Klaassen et al. 2012) that emission from CO may potentially trace a remnant, momentum-driven, outflow cavity that is no longer being actively driven by the central star. In comparison, SiO, which requires a fast shock and higher critical density to be excited, may be tracing an active outflow close to the central star. A major aim of this work is to explore systematic differences in the environment, age, and evolutionary nature between massive star-forming regions hosting outflows traced by both CO and SiO emission (i.e. potentially active outflows) compared with regions that have an outflow traced by CO and show no associated SiO emission (i.e. potentially momentum-driven fossil outflows).

In addition, we purposely observed the dense-gas tracer HCO^+ as a means of probing the infall dynamics in these regions. Infall is believed to form an important role in the high-mass star-formation process. However, exactly how mass is accumulated on the clump/cloud scales and finally accreted on to the central cores in massive star-forming regions is still unclear (e.g. see Motte, Bontemps & Louvet 2017 for a recent review). There are two dominant theoretical scenarios for the formation of massive stars: turbulent core accretion (McKee & Tan 2003) and competitive accretion (Bonnell et al. 2001). In the former, the infall dynamics would likely be localized on individual core/binary type scales, whereas in the latter the cloud and high-mass protostars form simultaneously (e.g. Tigé et al. 2017) and global collapse on clump/cloud scales is expected. In this formation scheme, the gas is likely to be channelled along converging flows on to central clouds that are undergoing global collapse on parsec scales. Several recent observations (e.g. Peretto et al. 2014; Williams et al. 2018) have observed velocity gradients along filamentary structures converging on to a central hub. In the observations presented here, we expect to probe signatures of global infall on scales of 1–2 pc, if present.

We present the results of an HCO^+, $H^{13}CO^+ J$=4–3, and SiO J=8–7 molecular line survey performed using the James Clerk Maxwell Telescope (JCMT) towards a sample of 33 high-mass star-forming regions selected from the Red MSX source (RMS) MSX survey (Lumsden et al. 2013). In Section 2 we summarize the observations presented in this paper. The results are presented in Section 3, the discussion in Section 4, and the main conclusions of the work are outlined in Section 5.

2 SAMPLE AND OBSERVATIONS

2.1 Sample selection

The sample includes 33 massive star-forming regions, selected from a previous outflow survey by Maud et al. (2015b), where 27 of the sources observed have an outflow detection traced by ^{12}CO (3–2). For completeness, we also include six regions that have no confirmed ^{12}CO (3–2) outflow detection in Maud et al. (2015b), but have associated $C^{18}O$ (3–2) emission (see Maud et al. 2015a) and therefore retain a dense massive core. All sources are part of the RMS survey and were selected to probe both evolutionary nature and cover a range in luminosity. The sample includes 20 YSOs, 11 compact H II and two H II/YSO RMS classified regions (Lumsden

et al. 2013). Objects labelled as H II/YSO regions were found to display characteristics of both YSOs and compact H II regions (see Lumsden et al. 2013 for a full discussion of the classification of RMS sources.). Furthermore, the source selection was chosen to be distance limited (<4.5 kpc) to minimize distance-related bias. However, since the observations were undertaken, the distances of two sources, G020.7617 and G045.0711, have been corrected. The distance to G020.7617 has been updated to the far kinematic distance of 11.8 kpc, and the distance to G045.0711 has been corrected to 7.75 ± 0.4 kpc (Wu et al. 2014; obtained from parallax and proper motion measurements). To keep the sample distance limited we omit these sources from the remaining analysis. Table 1 presents the source properties taken from the RMS survey. The sources are labelled by their RMS name (Column 1), and properties such as the RMS survey classification (e.g. YSO and H II), source V_{LSR}, distance, and bolometric luminosity are given. Where possible the *IRAS* name and/or more commonly used name(s) for each source are provided.

2.2 JCMT observations

SiO J=8–7, $H^{13}CO^+ J$=4–3, and $HCO^+ J$=4–3 were observed using the Heterodyne Array Receiver program (HARP) (Buckle et al. 2009) at the 15 m JCMT[1] as part of the projects M09AU18 (SiO J=8–7 and $H^{13}CO^+ J$=4–3) and M10AU04 ($HCO^+ J$=4–3). Due to time limitations, only 25 sources were observed as part of project M10AU04 ($HCO^+ J$=4–3). Project M09AU18 was observed between 2009/04/12 and 2010/04/05, and project M10AU04 between 2010 /04/16 and 2010/09/01. The HARP array consists of 16 receiver elements but during both projects receiver H14 was not operational and is subsequently missing from the data. The observations were taken in position-switched jiggle chop mode (Buckle et al. 2009), creating ∼ 2 arcmin by 2 arcmin maps. We observed each source for between 30 and 60 min, and the pointing was checked every hour on a known bright molecular source and is accurate to within ∼5 arcsec. $H^{13}CO^+$ and SiO were observed simultaneously in the same frequency set-up, where the Auto-Correlation Spectral Imaging System (ACSIS) was configured with an operational bandwidth of 1000 MHz×2048 channels, providing a velocity resolution of 0.42 km s^{-1}. For HCO^+ the bandwidth was set-up at 250 MHz×4096 channels, providing a velocity resolution of 0.05 km s^{-1}. At the observed frequency range of ∼345 GHz the JCMT has a beam size of ∼15 arcsec. The average atmospheric opacity ($\tau_{(225GHz)}$) obtained from the Caltech Submillimeter Observatory (CSO) during both sets of observations was 0.07.

The HARP/ACSIS data reduction was undertaken using the Starlink software packages SMURF, KAPPA, and GAIA (Jenness et al. 2015). The data were initially converted to spectral (RA-DEC-velocity) cubes using the SMURF command MAKECUBE. The data were gridded on to cubes with a pixel size of 7.5 arcsec by 7.5 arcsec using the function 'SincSinc', which is a weighting function using a sinc(πxsinc$k\pi x$) kernel. The noisy channels at the edges of the band were removed, and a linear baseline was subtracted. The data were converted from the antenna temperature scale T_A^* (Kutner & Ulich 1981) to main-beam brightness temperature T_{mb} using $T_{mb} = T_A^*/\eta_{mb}$, where the main beam efficiency η_{mb} has

---

[1] The JCMT has historically been operated by the Joint Astronomy Centre on behalf of the Science and Technology Facilities Council of the United Kingdom, the National Research Council of Canada, and the Netherlands Organization for Scientific Research.

Table 1. Source parameters for all objects in the sample taken from the RMS survey online archive.

Source Name	RMS Classification	RA (J2000)	Dec. (J2000)	V_{LSR} (km s^{-1})	Distance (kpc)	Luminosity (L$_\odot$)	*IRAS*/common name
			CO outflow detection[a]				
G010.8411−02.5919	YSO	18:19:12.09	− 20:47:30.9	12.3	1.9	2.4e+04	18162−2048
G012.9090−00.2607	YSO	18:14:39.56	− 17:52:02.3	36.7	2.4	3.2e+04	18117−1753/ W33A
G013.6562−00.5997	YSO	18:17:24.38	− 17:22:14.8	47.4	4.1	1.4e+04	18144−1723
G017.6380+00.1566	YSO	18:22:26.37	− 13:30:12.0	22.1	2.2	1.0e+05	18196−1331
G018.3412+01.7681	YSO	18:17:58.11	− 12:07:24.8	33.1	2.8	2.2e+04	18151−1208
G020.7617−00.0638	H II/YSO	18:29:12.36	− 10:50:38.4	56.9	11.8[b]	1.3/3.6e+04	
G043.3061−00.2106[c]	H II	19:11:16.97	+ 09:07:28.9	59.6	4.4	1.1e+04	19088+0902
G045.0711+00.1325	H II	19:13:22.10	+ 10:50:53.4	59.2	7.8[b]	6.2e+05	19110+1045
G050.2213−00.6063	YSO	19:25:57.77	+ 15:02:59.6	40.6	3.3	1.3e+04	19236+1456
G078.1224+03.6320	YSO	20:14:25.86	+ 41:13:36.3	− 3.9	1.4	4.0e+03	20126+4104
G079.1272+02.2782	YSO	20:23:23.83	+ 41:17:39.3	− 2.0	1.4	1.6e+03	20216+4107
G079.8749+01.1821	H II	20:30:27.45	+ 41:15:58.5	− 4.3	1.4	1.1e+03	20286+4105
G081.7133+00.5589	H II	20:39:02.36	+ 42:21:58.7	− 3.8	1.4	1.9e+03	
G081.7220+00.5699	H II	20:39:01.01	+ 42:22:50.2	− 4.7	1.4	1.2e+04	DR21 OH
G081.7522+00.5906	YSO	20:39:01.98	+ 42:24:59.1	− 4.0	1.4	9.0e+03	
G081.7624+00.5916	YSO	20:39:03.72	+ 42:25:29.6	− 4.4	1.4	2.6e+03	
G081.8652+00.7800	YSO	20:38:35.36	+ 42:37:13.7	9.4	1.4	3.6e+03	
G081.8789+00.7822	H II	20:38:37.71	+ 42:37:58.6	8.1	1.4	1.1e+04	
G083.0936+03.2724	H II	20:31:35.44	+ 45:05:45.8	− 3.1	1.4	1.2e+04	
G083.7071+03.2817	YSO	20:33:36.51	+ 45:35:44.0	− 3.6	1.4	3.9e+03	
G083.7962+03.3058	H II	20:33:48.02	+ 45:40:54.5	− 4.3	1.4	4.8e+03	
G103.8744+01.8558	YSO	22:15:09.08	+ 58:49:07.8	− 18.3	1.6	6.8e+03	22134+5834
G109.8715+02.1156	YSO	22:56:17.98	+ 62:01:49.7	− 11.1	0.7	1.5e+04	22543+6145/Cep A
G192.6005−00.0479	YSO	06:12:54.01	+ 17:59:23.1	7.4	2.0	4.5e+04	06099+1800/ S255 IR
G194.9349−01.2224	YSO	06:13:16.14	+ 15:22:43.3	15.9	2.0	3.0e+03	06103+1523
G203.3166+02.0564	YSO	06:41:10.15	+ 09:29:33.6	7.4	0.7	1.8e+03	06384+0932/NGC2264-C
G207.2654−01.8080	H II/YSO	06:34:37.74	+ 04:12:44.2	12.6	1.0	1.3/9.1e+03	06319+0415
			No CO outflow detection[a]				
G080.8645+00.4197	H II	20:36:52.16	+ 41:36:24.0	− 3.1	1.4	9.1e+03	
G080.9383−00.1268	H II	20:39:25.91	+ 41:20:01.6	− 2.0	1.4	3.2e+04	
G081.7131+00.5792	YSO	20:38:57.19	+ 42:22:40.9	− 3.6	1.4	4.9e+03	
G196.4542−01.6777	YSO	06:14:37.06	+ 13:49:36.4	18.0	4.1[b]	5.4e+04	06117+1350
G217.3771−00.0828	H II	06:59:15.73	− 03:59:37.1	25.1	1.3	8.0e+03	06567−0355
G233.8306−00.1803	YSO	07:30:16.72	− 18:35:49.1	44.6	3.3	1.3e+04	07280−1829

Notes. [a]The CO outflow sources have either a confirmed ^{12}CO(3–2) outflow or in the case of two sources, G017.6380 and G083.7962, show evidence of an outflow, whereas the No CO outflow sources have no observed emission consistent with an outflow in Maud et al. (2015b).

[b]The distance to G020.7617 has been updated to the far distance since the observations were undertaken. A distance of 7.75 ± 0.4 kpc to G045.0711 has recently been identified through measurements of parallax and proper motions by Wu et al. (2014). The distance to G196.4542 has been since updated to $4.05^{+0.65}_{-0.49}$ kpc (Asaki et al. 2014). The corrected distances for these sources are used in the remainder of the analysis.

[c]G043.3061−00.2106 was observed as part of the ^{12}CO outflow survey (Maud et al. 2015b). However, as G043.3061−00.2106 was not observed in the C^{18}O core properties survey by Maud et al. (2015a), this source was subsequently excluded from the ^{12}CO (3–2) outflow survey (Maud et al. 2015b). Inspection of the ^{12}CO (3–2) data shows emission indicative of outflow motions, thus we include this source as a CO outflow candidate in this work.

a value of 0.61 (Buckle et al. 2009). To increase the signal-to-noise ratio of the SiO (8–7) line, we re-sampled the velocity resolution to 1.68 km s^{-1} using the KAPPA command SQORST. The 1σ rms $T_{mb(rms)}$ per channel was determined from line-free channels excluding any noisy pixels towards the edges of the map; the typical values are 0.08 K, 0.04 K, and 0.6 K for H^{13}CO$^+$(0.42 km s^{-1}), SiO (1.68 km s^{-1}), and HCO$^+$(0.05 km s^{-1}), respectively. As mentioned in the previous section, the HCO$^+$ observations were not completed towards all sources in this survey; sources that were not observed are noted in Table 2.

with the ESA *Herschel Space Observatory*[2] (Pilbratt et al. 2010) using the PACS instrument (Poglitsch et al. 2010), were obtained from the *Herschel* archive in standard product generation form. The majority of the data were taken from the HOBYS (Motte et al. 2010) or HiGal (Molinari et al. 2010) surveys. Only two regions, G018.3412 and G078.1224, were not observed as part of these two surveys, and were observed under the PIs: Krauss (observation ID:1342191813) and Cesaroni (observation ID:1342211514), respectively (see Table 2 for a summary of the sources covered.).

2.3 Archival data

To complement the JCMT HARP observations, we utilize archival far-infrared (IR) data. The far-IR 70 µm observations, performed

[2] *Herschel* is an ESA space observatory with science instruments provided by European-led Principal Investigator consortia and with important participation from NASA.

Table 2. Summary of the molecular-line detections towards the sources surveyed. Column 1 gives the RMS name; sources where a $H^{13}CO^+$ component was detected more than 14.5 arcsec offset from the RMS source position are labelled RMS name-OFFSET. Column 2 gives the RMS classification of the source. Columns 3, 4, and 5 give the corresponding detection (Y), non-detection (N) or were not observed (–) of SiO, $H^{13}CO^+$, and HCO$^+$, respectively. Columns 6 and 7 are the asymmetries estimated from the $H^{13}CO^+$ and HCO$^+$ spectra extracted from both the average emission over the whole source and peak of the $H^{13}CO^+$ emission, where N, R and B represent no asymmetry, red asymmetry, and blue asymmetry, respectively. Column 8 is the detection (Y), and non-detection (N) of *Herschel* 70 μm, within 14.5 arcsec of the peak of the $H^{13}CO^+$ component. Sources not available or present in the online data by either survey are noted by the symbol (–).

Source Name	RMS Type	SiO (8–7)	$H^{13}CO^+$ (4–3)	HCO$^+$ (4–3)	Line Asymmetry[a] Average	Peak	*Herschel* 70 μm flux
				CO outflow detection			
G010.8411	YSO	N	Y	Y	N	N	–
G012.9090	YSO	Y	Y	Y	N	N	Y
G013.6562	YSO	Y	Y	Y	R	N	Y
G017.6380	YSO	N	Y	Y	N	B	Y
G018.3412	YSO	Y	Y	Y	N	N	Y
G043.3061	H II	Y	Y	Y	B	R	Y
G050.2213	YSO	Y	Y	Y	N	N	Y
G078.1224	YSO	Y	Y	Y	N	N	Y
G079.1272	YSO	Y	Y	Y	N	N	Y
G079.8749	H II	N	Y	Y	R	R	Y
G079.8749-OFFSET	–	N	Y	Y	N	B	Y
G081.7133	H II	Y	Y	Y	–	–	Y
G081.7220	H II	Y	Y	Y	B	B	Y
G081.7522	YSO	Y	Y	–	–	–	Y
G081.7522-OFFSET	–	N	Y	–	–	–	Y
G081.7624	YSO	N	N	–	–	–	Y
G081.7624-OFFSET	–	Y	Y	–	–	–	Y
G081.8652[b]	YSO	N	N	Y	–	–	N[c]
W75N[b]	–	Y	Y	Y	R	N	Y
G081.8789[b]	H II	N	N	Y	–	–	N[c]
G083.0936	H II	N	Y	Y	N	N	–
G083.7071	YSO	N	N	Y	N	N	–
G083.7071-OFFSET	–	N	Y	Y	N	B	–
G083.7962	H II	N	Y	Y	R	N	–
G103.8744	YSO	N	Y	Y	N	B	Y
G109.8715	YSO	Y	Y	Y	N	B	Y
G192.6005	YSO	Y	Y	Y	N	N	Y
G194.9349	YSO	N	Y	Y	N	N	Y
G203.3166	YSO	Y	Y	Y	R	R	Y
G203.3166-OFFSET	–	Y	Y	Y	B	N	Y
G207.2654	H II/YSO	Y	Y	Y	N	N	Y
				No CO outflow detection			
G080.8645	H II	N	Y	–	–	–	Y
G080.9383	H II	N	N	–	–	–	Y
G081.7131	YSO	N	N	–	–	–	Y
G196.4542	YSO	N	Y	Y	N	N	–
G217.3771	H II	N	Y	–	–	–	Y
G233.8306	YSO	N	N	–	–	–	Y

Notes. [a]The line asymmetry is given for both the average and peak emission, and is denoted by a B for a blue asymmetry where $\delta V \leq -0.25$, R for red asymmetry where $\delta V \geq 0.25$, and N for no asymmetry.
[b]These sources are all spatially located within $\sim$1 arcmin. The $H^{13}CO^+$ emission peaks between the two RMS sources, $\sim$ 40 arcsec from G081.8789, and $\sim$20 arcsec from G081.8652. While $H^{13}CO^+$ emission does extend over the whole region, there appears to be no obvious extension or enhancement towards either RMS source, therefore the $H^{13}CO^+$ component is associated with the offset position, W75N, and G081.8789 and G081.8652 are classed as non-detections and their HCO$^+$ properties are not estimated.
[c]*Herschel* 70 μm emission extends over both sources; however the dendrogram fit cannot separate the emission from the dominant 70 μm component in the field which is associated with the offset position, W75N.

3 RESULTS

3.1 Determining the source extents and properties from the HCO$^+$ and $H^{13}CO^+$ emission

The extent of the $H^{13}CO^+$ emission is determined from dendrogram fits made to the $H^{13}CO^+$ zeroth-order moment maps, using the PYTHON-based dendrogram fitting application, ASTRODENDRO. An

$H^{13}CO^+$ detection is assigned based on a $\geq 5\sigma$ detection over a minimum of four contiguous pixels (approximately equivalent to the beam area of 4.45 pixels). The rms noise per pixel in the integrated intensity maps is obtained using $\Delta I = T_{mb(rms)} \Delta v \sqrt{N_{chan}}$, where $T_{mb(rms)}$ is the rms noise level in K per channel, Δv is the velocity resolution in km s^{-1}(0.42 km s^{-1} for $H^{13}CO^+$), and N_{chan} is the number of channels used to integrate the emission. The number of channels is determined from the minimum and maximum
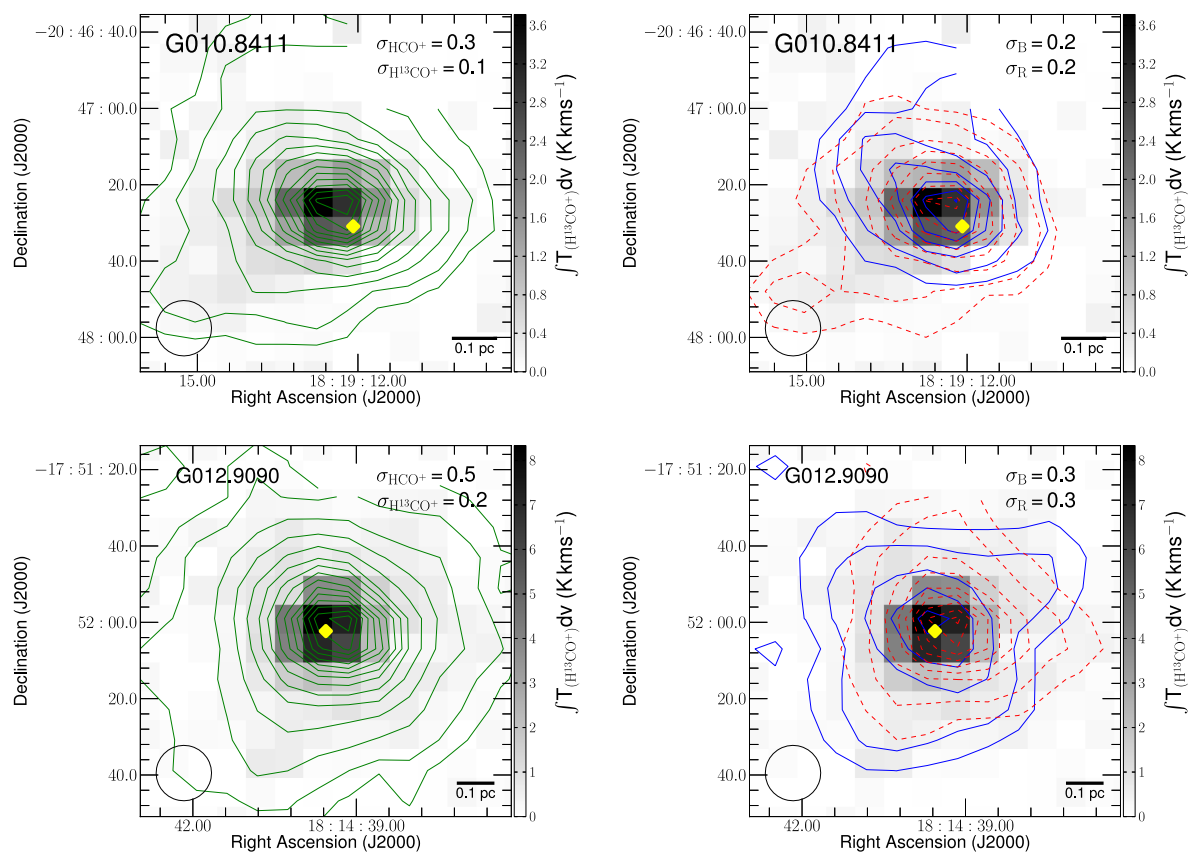
Figure 1. $H^{13}CO^+$ and HCO^+ zeroth-order moment maps. The $H^{13}CO^+$ maps are shown in grey-scale and are the total integrated emission ($\int T_{mb} dv$ in units of K. km s^{-1}), integrated from the minimum to maximum channels with 3σ emission. The yellow diamonds mark the RMS source positions. The JCMT beam is shown in the bottom left corner, and the source name is shown in the top left corner. Left: the HCO^+ emission is overlaid in green solid contours for the total moment maps (again integrated from the minimum and maximum channels with 3σ emission in the HCO^+ maps) where the 1σ rms (in units of K. km s^{-1}) for the HCO^+ (σ_{HCO^+}) and the $H^{13}CO^+$ ($\sigma_{H^{13}CO^+}$) integrated intensity maps are given in the top right corner. The HCO^+ contour levels are from $1\sigma \times(5,10,20,...$ to peak in-steps of 10σ). Right: the red- and blue-shifted HCO^+ emission is shown by the red (dashed) and blue (solid) contours, respectively. The blue- and red-shifted contours are taken from the minimum and maximum channels with 3σ emission, respectively, excluding the central emission which is defined by the $H^{13}CO^+$ FWHM (see Table A1 for the $H^{13}CO^+$ FWHM values). The 1σ levels for the red- (σ_R) and blue-shifted (σ_B) emission are given in the top right corner, where the contour levels are from $1\sigma \times(5,10,20,...$ to peak in-steps of 10σ). The velocity ranges used to integrate the HCO^+ emission are $9.5-15.6$ km s^{-1} for G010.8411, and $30.3-44.0$ km s^{-1} for G012.9090. The remainder of the sources are presented in the online data.

velocity in the $H^{13}CO^+$ cubes that contain emission above the 3σ limit. A sample of the $H^{13}CO^+$ zeroth-order moment maps with the HCO^+ emission overlaid is shown in Fig. 1 with the remainder provided in the online data. The HCO^+ and $H^{13}CO^+$ spectra (shown in Fig. 2) display the average emission per pixel extracted from the sum of all pixels within the $H^{13}CO^+$ dendrogram fitted mask. The Gaussian fits of the $H^{13}CO^+$ spectra, presented in Table A1 of the Appendix, are extracted from the sum of the emission over the region.

We detect $H^{13}CO^+$ emission towards 28 of the 31 distance-limited RMS sources observed. For the three undetected sources (G233.8306, G081.7131, and G083.9383) no $H^{13}CO^+$ emission is detected in a single pixel above the 3σ limit. Towards several sources we find the peak of the $H^{13}CO^+$ emission is offset by more than the full width at half-maximum (FWHM) of the JCMT beam (>14.5 arcsec) from the RMS position. Furthermore, towards two sources, G081.7522 and G203.3166, two $H^{13}CO^+$ features are identified in the dendrogram fit. One component is associated with the RMS source position and a second structure is located in an offset position (>14.5 arcsec from the RMS position). We discuss the offset components in more detail below.

3.1.1 $H^{13}CO^+$ offset components

An offset component is identified if the centre of the pixel containing the peak of the $H^{13}CO^+$ integrated intensity emission is spatially offset by more than a beam FWHM (14.5 arcsec) from the RMS source position (see Fig. B1 in the online data for the HCO^+ and $H^{13}CO^+$ zeroth-order moment maps towards the offset sources). In total, six $H^{13}CO^+$ offset components are identified.

(i) Towards G079.8749, only one $H^{13}CO^+$ component is identified and is offset from the RMS source position by $\sim$24 arcsec, located at R.A. (J2000) $20^h30^m29^s.5$, Dec. (J2000) $+41°15'51''.4$. However, there is a clear enhancement in the $H^{13}CO^+$ emission towards the RMS source position in agreement with previous ammonia VLA observations (Lu et al. 2014). We therefore split the $H^{13}CO^+$ emission into two separate components, a smaller one associated with the RMS source position, and a second larger component located in the offset position now labelled G079.8749-OFFSET.

(ii) Towards G081.7522, two $H^{13}CO^+$ components are identified: one feature coincident with the RMS source position and a second offset by $\sim$30 arcsec to the south of the RMS position located at
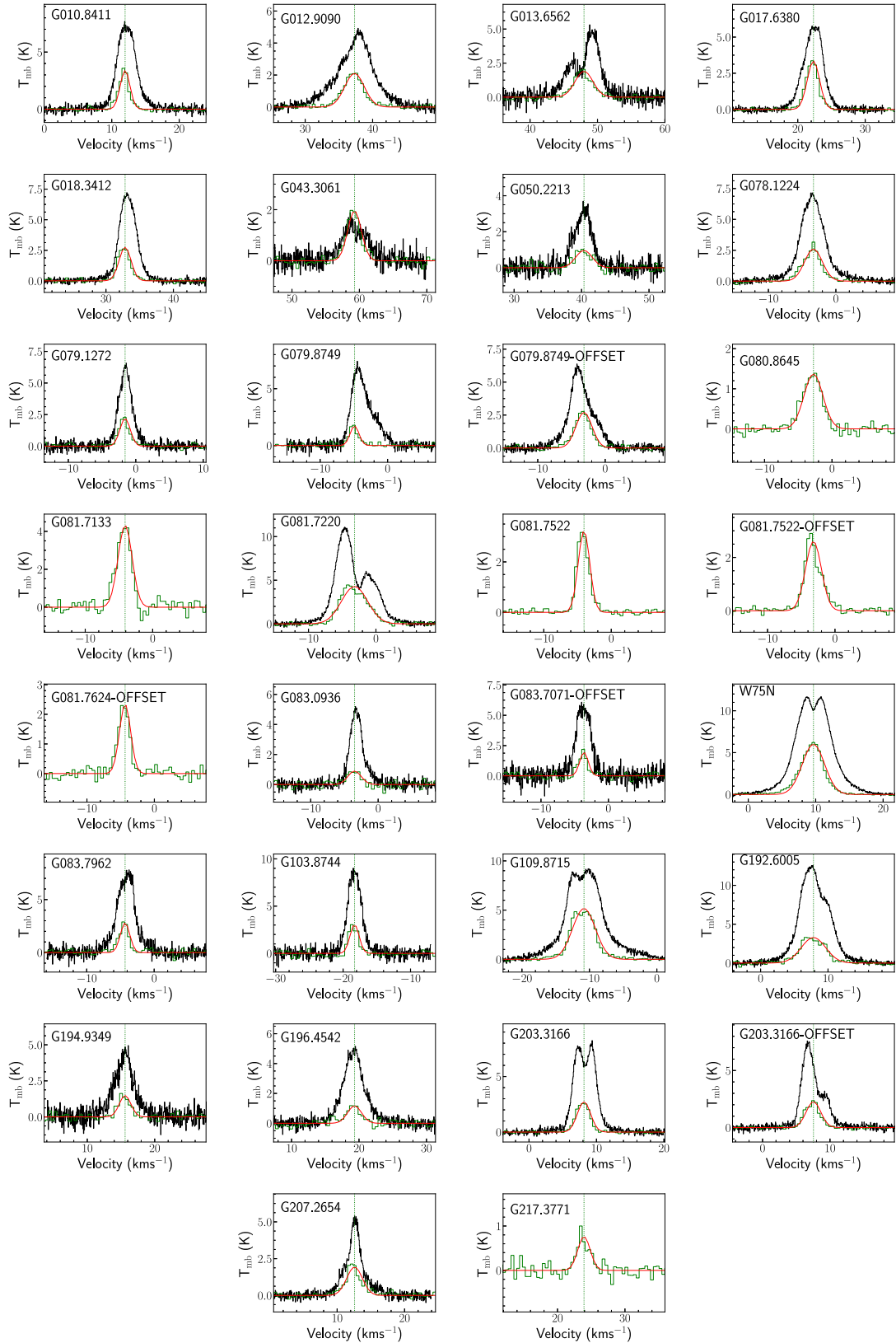
Figure 2. HCO$^+$ (solid black line) and H^{13}CO$^+$ (solid green line) $J = 4–3$ spectra averaged over all pixels within the dendrogram fitted masks. The solid red line shows the Gaussian fits to the H^{13}CO$^+$ emission (calculated from Table A1 of the Appendix). The green dotted line is at the position of the H^{13}CO$^+$ V_{LSR} taken from Table A1. Both the H^{13}CO$^+$ spectra and respective Gaussian fit have been multiplied by a factor of 4. The velocity scale is the same for all plots, and is H^{13}CO$^+$ $V_{LSR} \pm 12 \, km \, s^{-1}$. Sources where no HCO$^+$ observations were undertaken are missing the HCO$^+$ spectra.

R.A. (J2000) $20^h39^m00\overset{s}{.}3$, Dec. (J2000) $+42°24'36\overset{''}{.}4$. We label the second offset component G081.7522-OFFSET. This source, located in the northern part of the DR 21 filament, was identified as a mm-continuum source (N43) by Motte et al. (2007) and does not have an outflow association in either SiO (2–1) (Motte et al. 2007) or CO (2–1) (Schneider et al. 2010).

(iii) Towards G081.7624, only one $H^{13}CO^+$ component is present, located ~22 arcsec to the north of the RMS source position at R.A. (J2000) $20^h39^m03\overset{s}{.}3$, Dec. (J2000) $+42°25'50\overset{''}{.}6$, and is now labelled G081.7624-OFFSET. This component also resides in the northern part of the DR 21 filament and was identified as a mm-continuum source (N53) by Motte et al. (2007). This $H^{13}CO^+$ feature has associated SiO (2–1) emission (Motte et al. 2007) and a CO (2–1) outflow (Schneider et al. 2010). Furthermore, the ^{12}CO (3–2) emission in Maud et al. (2015b) is also coincident with the offset component and we associate the outflow properties to G081.7624-OFFSET in this work.

(iv) For G081.8789 and G081.8652, which were observed in the same JCMT map, the dendrogram fit reveals only one $H^{13}CO^+$ feature, located between the two RMS positions, ~40 arcsec from G081.8789, and ~20 arcsec from G081.8652 at R.A. (J2000) $20^h38^m36\overset{s}{.}3$, Dec. (J2000) $+42°37'30\overset{''}{.}3$. While $H^{13}CO^+$ emission extends over both sources, there appears to be no obvious enhancement towards either RMS source; this is consistent with the $C^{18}O$ emission in this region (Maud et al. 2015a). The peak of the $H^{13}CO^+$ emission is coincident with W75N, which hosts multiple mm continuum peaks and outflow emission (e.g. Minh et al. 2010). Furthermore, the ^{12}CO (3–2) emission in Maud et al. (2015b) is also coincident with W75N and we associate the outflow properties to W75N in this work. Given the source confusion in this field, W75N was not listed as an MSX point source. We label this $H^{13}CO^+$ component as W75N but class it as an offset source for the remainder of the analysis as it does not coincide with a listed RMS point source position.

(v) Towards G083.7071, only one $H^{13}CO^+$ component is identified, offset from the RMS position by ~16 arcsec. The peak of the $H^{13}CO^+$ emission is located at R.A. (J2000) $20^h33^m35\overset{s}{.}2$, Dec. (J2000) $+45°35'36\overset{''}{.}5$. This component is not coincident with any previously known source and is labelled G083.7071-OFFSET.

(vi) Towards G203.3166, two $H^{13}CO^+$ components are identified in the dendrogram fit: the first feature is coincident with the RMS source position and the second component is offset by ~37 arcsec to the south-east of the RMS position. The offset component, labelled G203.3166-OFFSET, is located at R.A. (J2000) $06^h41^m12\overset{s}{.}1$, Dec. (J2000) $+09°29'11\overset{''}{.}3$, and is coincident with the position of C-MM3 (see Cunningham et al. 2016 and references therein).

3.1.2 HCO$^+$ column density estimates

We estimate the HCO$^+$ column density assuming that the $H^{13}CO^+$ emission is optically thin, following,

$$N_{H^{13}CO^+} = \frac{8\pi\kappa\nu^2}{hc^3}\frac{1}{g_u A_{ul}}Q(T_{ex})e^{\frac{E_u}{kT_{ex}}}\int T_{mb}dv, \quad (1)$$

where $\int T_{mb}dv$ is either the average of the $H^{13}CO^+$ integrated intensity (where the emission is the average over all pixels in the dendrogram fit) or the peak $H^{13}CO^+$ integrated intensity extracted at the peak of the $H^{13}CO^+$ emission, and $N_{H^{13}CO^+}$ is then the average or peak column density. $Q(T_{ex})$ is the partition function, and is well approximated by $Q(T_{ex}) = (kT_{ex})/(hB)$ for linear rotators, where B is

the rotational constant and T_{ex} is the excitation temperature. A_{ul} is the Einstein A coefficient in s^{-1}, g_u is the degeneracy of the upper energy state, and E_u is the energy of the upper state. We assume a value of 44 K for the excitation temperature as used by Klaassen & Wilson (2007). Furthermore, towards a similar sample of RMS selected young massive star-forming regions (Cunningham 2015) an average rotational temperature of 44 K was derived from the CH_3CN ($J = 5$–4) ladder. The HCO$^+$ column densities are estimated assuming an abundance ratio between $H^{13}CO^+$ and HCO$^+$ to be 65 (Rygl et al. 2013) and are given in Table 3. In addition, we also provide mass estimates for individual sources in Table 3. The masses are taken from Maud et al. (2015a), derived using the 850 μm SCUBA fluxes. For sources not listed in Maud et al. (2015a), we follow the same procedure and extract the 850 μm fluxes from Di Francesco et al. (2008) checking that the SCUBA positions are coincident with the position of the offset emission. The mass estimates are used in Sections 4.2, 4.3, and 4.3.1 for comparison with the SiO luminosities, and are used in the bolometric-luminosity-to-mass ratio in Fig. 4.

3.2 Detecting active outflow signatures with SiO

A source is determined to have an SiO detection if a minimum 3σ detection is obtained in at least one pixel in the SiO integrated intensity maps. The integrated SiO intensity is extracted from the zeroth-order moment maps, where the velocity range is determined using either the velocity of the upper and lower channels above 3σ in the SiO channel maps (where possible) or from the ^{12}CO linewidths taken from Maud et al. (2015b). Furthermore, only pixels situated within the respective $H^{13}CO^+$ integrated intensity mask are considered (this was done to eliminate the possibility of a spurious detection that may appear towards the edge of the maps being identified as a detection.). The SiO luminosity (in units of K km s^{-1} kpc^2) is calculated from $L_{SiO} = \int T_{mb(SiO)}dv \times 4\pi d^2$, where $\int T_{(SiO)}dv$ is the SiO integrated intensity extracted from the sum of the pixels in the zeroth-order moment maps (see Table 3 for individual source values and Fig. B2 of the online data for individual SiO integrated intensity maps), and d is the distance to the respective source. For sources without an SiO detection, we estimate the 3σ upper limits using the rms in a single pixel. For the six sources without a CO outflow detection a velocity interval of 26 km s^{-1} (the average ^{12}CO linewidth of the SiO non-detections) is used to estimate the upper limit of the SiO luminosity.

SiO $J = 8$–7 is detected towards 14 (~45 per cent) of the 31 RMS sources observed (excluding both sources, G045.0711 and G020.7617, that fall outside of the distance limits). See Table 2 for a list of detections towards individual sources. We do not detect SiO emission towards the six sources without a confirmed CO outflow in Maud et al. (2015b). We detect SiO emission towards three of the six defined OFFSET sources, G203.3166-OFFSET, G081.7624-OFFSET and W75N. Therefore, we detect SiO emission, including the offset sources, towards 17 (46 per cent) of the distance-limited sample (see Table 4).

For completeness, we also provide an estimate of the average SiO column density (N_{SiO}) and average abundance (X_{SiO}) in Table 3. We calculate the SiO column density using equation (1) substituting the values for SiO (8–7). For the SiO abundance, we derive the N_{H_2} column density using the ^{12}CO (3–2) column densities given in Maud et al. (2015b), averaged over the blue- and red-shifted outflow lobes. The CO (3–2) column densities were used because the SiO emission is likely to be produced as a result of shocks in the

Table 3. Physical properties estimated for the sources. The 3σ upper limits (represented by $<$) are provided for sources that have no detected emission. The symbol (–) represents sources for which no estimate of the property was possible.

Source name	Peak N_{HCO^+} (cm^{-2}) ($\times 10^{13}$)	Average N_{HCO^+} (cm^{-2}) ($\times 10^{13}$)	Average N_{SiO} (cm^{-2}) ($\times 10^{12}$)	Average X_{SiO} ($\times 10^{-9}$)	Mass (M$_\odot$)	$\int T_{SiO}\,dv$ (K km s^{-1})
SiO detection						
G012.9090	24.2 ± 8.6	5.4 ± 2.4	3.4 ± 0.7	1.1 ± 0.2	1167	25.4
G013.6562	5.1 ± 0.7	4.5 ± 0.4	2.0 ± 0.4	0.5 ± 0.2	1385	5.2
G018.3412	12.1 ± 0.7	4.3 ± 0.3	1.6 ± 0.4	1.1 ± 0.2	224	1.0
G043.3061	4.8 ± 1.3	3.5 ± 0.4	0.8 ± 0.2	–	595	3.2
G050.2213	2.7 ± 0.9	2.1 ± 0.5	2.0 ± 0.4	2.5 ± 0.7	397	1.2
G078.1224	17.6 ± 0.8	6.1 ± 0.3	4.3 ± 0.7	6.7 ± 1.1	90	53.1
G079.1272	4.1 ± 0.7	3.0 ± 0.4	1.8 ± 0.2	5.4 ± 1.1	24	2.1
G081.7133	11.5 ± 1.3	8.0 ± 0.8	3.4 ± 0.7	1.8 ± 0.2	367	35.0
G081.7220	69.9 ± 2.0	15.2 ± 0.5	10.0 ± 1.3	18.0 ± 2.9	312	132.0
G081.7522	10.7 ± 0.8	4.9 ± 0.3	2.0 ± 0.7	1.1 ± 0.2	272	1.2
G081.7624-OFFSET	6.12 ± 0.9	3.4 ± 0.5	4.0 ± 0.7	3.6 ± 0.7	201	44.6
W75N	102.1 ± 1.5	17.5 ± 0.3	6.7 ± 0.2	2.5 ± 0.2	647	98.3
G109.8715	62.3 ± 1.4	15.4 ± 0.4	6.5 ± 0.9	1.8 ± 0.2	112	85.8
G192.6005	14.7 ± 1.0	10.5 ± 0.6	2.5 ± 0.7	3.4 ± 0.9	130	17.2
G203.3166	11.4 ± 0.8	4.7 ± 0.2	1.8 ± 0.5	19.8 ± 4.3	61	19.6
G203.3166-OFFSET	8.9 ± 0.6	4.3 ± 0.2	2.2 ± 0.4	–	33	11.8
G207.2654	7.1 ± 1.5	4.0 ± 0.5	2.2 ± 0.7	5.6 ± 1.4	172	4.4
SiO non-detection						
G010.8411	12.2 ± 1.5	4.3 ± 0.4	<1.3	–	139	<0.9
G017.6380	19.1 ± 0.7	5.4 ± 0.2	<1.3	–	374	<0.8
G079.8749	2.7 ± 0.7	2.0 ± 0.4	<1.1	–	–	<0.7
G079.8749-OFFSET	16.1 ± 1.3	5.7 ± 0.3	<1.1	–	–	<0.7
G081.7522-OFFSET	10.8 ± 1.0	5.4 ± 0.3	<1.3	–	–	<0.9
G083.0936	2.4 ± 1.3	1.6 ± 0.6	<0.9	–	–	<0.5
G083.7071-OFFSET	2.5 ± 0.9	2.2 ± 0.6	<1.3	–	–	<0.8
G083.7962	3.5 ± 0.9	3.5 ± 0.6	<1.3	–	–	<0.9
G103.8744	4.5 ± 1.1	3.7 ± 0.8	<1.6	–	91	<1.0
G194.9349	3.1 ± 0.9	2.3 ± 0.6	<1.3	–	–	<0.9
No SiO or CO outflow detected						
G080.8645	6.3 ± 0.7	3.4 ± 0.3	<1.3	–	137	<0.8
G196.4542	3.5 ± 0.9	2.1 ± 0.5	<1.6	–	167	<1.0
G217.3771	1.8 ± 0.9	1.2 ± 0.4	<1.3	–	–	<0.8

Table 4. Summary of the outflow and infall detections.

Source type	Total	SiO 3σ	Total HCO$^+$ observed	Blue asymmetric[a] profile	
				Ave	Peak
YSO	20	10	16	0	3
H II	10	3	6	2	1
H II/YSO	1	1	1	0	0
OFFSET	6	3	4	1	2
Total (per cent)	37	17(46 per cent)	27(73 per cent)	3(12 per cent)	6(24 per cent)

Notes. [a]The asymmetry is derived for 25 sources using the H^{13}CO$^+$ and HCO$^+$ emission extracted from both the average (Ave) and peak (Peak) spectra, where the average spectra are taken from the emission averaged over all pixels taken from the dendrogram fits and the peak spectra are taken from the pixel at the peak of the H^{13}CO$^+$ emission.

jet/outflow and is not expected to be associated with the compact continuum emission tracing the core. However, in doing this we also assume that SiO arises from the same component in the outflow as the CO emission, which may not be the case.

3.3 Infall signatures determined from the HCO$^+$ and H^{13}CO$^+$ emission

Both HCO$^+$ (4–3) and H^{13}CO$^+$ (4–3) are dense-gas tracers ($n_{crit} \sim 8 \times 10^6$ cm^{-3}) and, as such, their emission can be used

to probe the dynamics of the dense-gas, such as infall or expansion. Infall is typically interpreted if a blue asymmetry, either from a double-peaked line profile with a brighter blue peak or a single-peak profile, is observed in the optically thick HCO$^+$ transition, and is offset from the optically thin isotopologue, H^{13}CO$^+$, which shows only a single peaked component at rest velocity (e.g. Myers et al. 1996). A single-peak in the optically thin H^{13}CO$^+$(4–3) line allows us to distinguish between self-absorption and multiple line-of-sight components in the optically thick HCO$^+$ profile. The predominance of either a blue or red asymmetry is quantified by the skewness parameter (Mardones et al. 1997) which is estimated from:

$$\delta V = \frac{V_{\text{thick}} - V_{\text{thin}}}{\Delta V_{\text{thin}}}, \qquad (2)$$

where V_{thick} and V_{thin} are the LSR velocities at line peak for the optically thick HCO$^+$(4–3) and optically thin H^{13}CO$^+$(4–3) transitions, respectively. The velocity difference is then normalized by the FWHM of the optically thin H^{13}CO$^+$ line (ΔV_{thin}). The H^{13}CO$^+$ FWHM and V_{LSR} are taken from the Gaussian fits presented in Table A1 of the Appendix and V_{thick} is taken from the position of the brightest emission peak in the HCO$^+$ spectrum. To explore the presence of global infall in these regions, the spectra shown in Fig. 2 are extracted from the average of the emission over all pixels within the dendrogram-fitted masks. The result is then the dimensionless skewness parameter δV. A significant blue or red excess is defined as $\delta V \leq -0.25$ or $\delta V \geq 0.25$, respectively (Mardones et al. 1997). Of the sources where it was possible to determine the asymmetries, three objects show a blue excess indicative of infall and five show a red excess (expansion) and 17 show no red or blue excess. All three sources with a blue excess have a corresponding SiO detection and three of the five sources with a red excess have an SiO detection (see Table 2 for individual sources). The number of sources with an infall detection is consistent with the number of sources without an infall detection given the Poisson errors of 3 ± 1.7 and 5 ± 2.25, respectively. However, as the emission is extracted from the full source extent and likely encompasses multiple protostars, this may add noise and mask the signs of global infall. Therefore, we also assess the asymmetry considering the spectra from the H^{13}CO$^+$ peak position, finding a total of six sources (see Table 2) with a blue asymmetry and three with a red asymmetry. Only a single source G081.7220 displays a blue asymmetry in both the averaged and peak spectra. Furthermore, the Poisson errors are again consistent for sources displaying a blue and red asymmetry of 6 ± 2.5 and 3 ± 1.7, respectively. This suggests that the majority of sources in our sample show no preference for global infall motions. However, an important consideration is the sensitivity for infall asymmetry to line optical depth, excitation temperature, and density. Smith et al. (2013) find an increase in the blue asymmetry of the optically thick line with decreasing beam size, suggesting that matching the beam size with the energy of line transition will increase the detection of infall signatures. Furthermore, as noted we are likely sensitive to multiple sources within the JCMT beam which can add noise to the observations. Future higher spatial resolution observations, resolving individual protostars, will be able to directly test this. It should also be noted that HCO$^+$ is a known tracer of outflow emission in massive star-forming regions (e.g. Walker-Smith et al. 2014), and several of the regions display broad-line wings in the HCO$^+$ spectra which can be clearly seen in Fig. 2 (e.g. G109.8715). In addition, several sources show an offset between the red- and blue-shifted HCO$^+$ emission in Fig. B1 of the online data (e.g. G050.2213, G192.6005, and G207.2654), again

suggesting that the HCO$^+$ emission is influenced by the outflow in several regions. Furthermore, sources that display no asymmetric line profile in the HCO$^+$ spectra, taken over the whole source extent, but show a blue asymmetric profile in the spectra taken from the peak, tend to show multiple components in the red- and blue-shifted HCO$^+$ emission maps (e.g. G017.6562 and G083.7071-OFFSET). This may add to the lack of consistency between the presence of asymmetry in the peak and average spectral line profiles.

3.4 Far-IR associations

We obtain 70 µm *Herschel* PACS fluxes for 25 of the 31 RMS sources with available data in the archive. The 70 µm flux was extracted using dendrogram fits, again using the PYTHON package ASTRODENDRO. The minimum number of contiguous pixels was set to the beam area of the *Herschel* map and the minimum detection was set to 5σ. The rms noise for each source was determined from an aperture local to that source and not from the entire map' therefore larger regions with higher levels of emission may have higher noise estimates. We assign *Herschel* 70 µm emission to an H^{13}CO$^+$ component if the peak of the 70 µm emission is within 14.5 arcsec of the peak of the H^{13}CO$^+$ component (see Table 2 for the association of a 70 µm component with a respective H^{13}CO$^+$ component.). Of the 25 RMS sources with available *Herschel* 70 µm data, 23 have an associated *Herschel* peak. Only G081.8652 and G081.8789 do not have an associated 70 µm component. However, as with the H^{13}CO$^+$ emission towards these sources, 70 µm emission extends over both RMS source positions but there is no obvious enhancement towards either RMS source and the peak of the 70 µm emission coincides with the offset H^{13}CO$^+$ component, W75N. All of the OFFSET sources have an associated 70 µm component within 14.5 arcsec of the identified H^{13}CO$^+$ peak.[3] The sum of the 70 µm flux, within the dendrogram mask, is converted to a luminosity through $L_{70\,\mu m} = 4\pi d^2 \times F_{70\,\mu m}$, using a 25 µm bandwidth for the *Herschel* 70 µm PACS filter.

4 DISCUSSION

4.1 Comparison of SiO-detected and non-detected source properties

SiO emission is detected towards approximately 46 per cent of the sources. Table 5 presents the average, median, and standard deviation of the source properties (e.g. bolometric luminosity, distance, and HCO$^+$ column density) for the SiO-detected and non-detected samples. For completeness we also include sources without an SiO or a CO outflow detection. We perform Kolmogorov–Smirnoff (KS) tests to determine if the source properties of the SiO-detected and non-detected sources are drawn from the same underlying distribution. The returned *p*-value from the KS test gives the confidence level at which the null hypothesis (i.e. that the two samples originate from the same underlying distribution) can be rejected. A value of ≤ 0.01 is associated with a high confidence that the two populations originate from different underlying distributions. We find no difference in the distance to sources with or without an SiO detection. The median distance is 1.4 kpc for both samples. If the emission traced by SiO is considerably smaller than the beam, suggesting a very

---

[3] It should be noted that for G203.3166-OFFSET when observed at higher spatial resolution (e.g. Cunningham et al. 2016) the 70 µm emission is not directly associated with the offset position C-MM3

Table 5. Summary of properties between SiO-detected and non-detected sources.

Source properties	SiO-detected[a]		No SiO detected[a]		No SiO or CO detected[a]		KS test[b]	
	Mean	Median	Mean	Median	Mean	Median	No SiO	No SiO or CO
Distance (kpc)	1.9 ± 1.1	1.4	1.6 ± 0.3	1.4	2.1 ± 1.1	1.4	0.45	0.63
L_* ($L_\odot \times 10^3$)	13 ± 12	11	15 ± 27	5	20 ± 18	11	0.52	0.51
$H^{13}CO^+$ FWHM[c] (km s^{-1})	2.9 ± 0.8	2.7	2.0 ± 0.5	1.9	2.7 ± 0.5	2.5	0.05	0.11
$C^{18}O$ FWHM (km s^{-1})	2.9 ± 0.7	2.6	2.6 ± 0.7	2.7	–	–	0.48	–
$L_{70 \mu m}$ ($L_\odot \times 10^2$)	27 ± 30	18	17 ± 34	2	18 ± 15	10	0.21	0.33
Mass ($M_\odot$)	364 ± 378	224	201 ± 124	139	107 ± 64	137	0.91	0.18
Average N_{HCO^+} (cm$^{-2} \times 10^{13}$)	6.9 ± 4.7	4.7	3.6 ± 1.5	3.6	2.3 ± 0.9	2.1	0.29	0.06
Peak N_{HCO^+} (cm$^{-2} \times 10^{13}$)	22.1 ± 27.4	11.4	7.7 ± 6.0	4.2	3.9 ± 1.9	3.5	0.12	0.04
^{12}CO linewidth (km s^{-1})	48 ± 19	56	26 ± 6	25	–	–	0.009	–

Notes. [a]The mean is given with $\pm$ standard deviation. For the No SiO detected sample the mean and median values are estimated considering sources without an SiO-detection that have a CO outflow detection. For the No SiO or CO detected column the mean and median values are estimated considering only those sources with no SiO and no CO outflow.
[b]The results of the KS test for the No SiO column is considering sources with and without and SiO detection that have a CO outflow detection. The No SiO or CO is considering all sources without an SiO detection, including those sources with no CO outflow in Maud et al. (2015b).
[c]The H$^{13}CO^+$ FWHM presented here is extracted from the dendrogram fits to the full source extent.

young outflow, then beam dilution may be responsible for the remainder of the SiO non-detections. However, this would need to be tested with higher angular resolution observations. We note that several of the SiO non-detections have the weakest H$^{13}CO^+$ emission in the sample, but there is no obvious difference in the masses or bolometric luminosities between populations. Therefore, the lack of an SiO detection towards these sources should not be due to sensitivity limitations in the sample.

We find no significant differences between the source properties of the SiO-detected and SiO non-detected populations (see Table 5 for a list of all returned *p*-values.). If we compare the outflow properties taken from Maud et al. (2015b), such as the outflow velocity, momentum, force, mass, and energy, we find only the CO outflow velocity has a *p*-value ≤ 0.01 between the SiO-detected and SiO non-detected sample. Furthermore, only sources with an SiO detection have a $^{12}CO\,(3–2)$ total linewidth >35 km s^{-1}, suggesting SiO emission is a more efficient tracer of high-velocity outflows. This is consistent with the CO outflow velocity ranges observed by Gibb et al. (2007) towards a sample of young massive stars, where sources with detected SiO (5–4) have associated outflows with a total maximum CO velocity of >36 km s^{-1}. This suggests that the detection of the higher *J* transitions of SiO is an indication of the presence of a high-velocity outflow and is consistent with the expected shock velocities (>25 km s^{-1}) required to disrupt dust grains (e.g. Schilke et al. 1997). For the remaining CO outflow properties, we find no difference between the SiO-detected and non-detected samples. However, we find the total outflow-mass between the two populations has a *p*-value≥ 0.9999, thus the outflow-masses estimated from the CO emission are drawn from the same distribution.

4.2 SiO luminosity as a function of source properties

We perform Spearman rank correlations along with linear regression fits to the estimated source properties as a function of the SiO luminosity with the outcomes presented in Table 6. We assume that a correlation is significant, given the small sample sizes, if a *p*-value of ≤ 0.01 is found and a correlation coefficient (*R*) of >0.53 is obtained. The H$^{13}CO^+$ FWHM, HCO$^+$ column density (both the peak and average), ^{12}CO (3–2) total linewidth or outflow velocity, outflow force and energy are all found to correlate with the SiO luminosity and are presented in Fig. 3. We find no correlation

among the bolometric luminosity, source mass, outflow-mass, and momentum with the SiO luminosity.

The correlation of the SiO luminosity with the H$^{13}CO^+$ FWHM was also observed by Klaassen et al. (2012) in their sample of high-mass star-forming regions. Furthermore, for both the SiO-detected and non-detected sources, the H$^{13}CO^+$ FWHM is greater than would be estimated considering only the linewidth–size relation (Larson 1981), and may then be a measure of the turbulence in these regions. This would suggest an increase in turbulence with increasing SiO luminosity, which may be a product of the shocks associated with the production of SiO. However, no correlation is observed between the C^{18}O FWHM from Maud et al. (2015a) and the SiO luminosity. Towards several sources (e.g. G050.2213, G192.6005, and G207.2654) the HCO$^+$ red- and blue-shifted emission (see Fig. B1 in the online data) appears to be offset, indicating the HCO$^+$ emission is tracing the outflows in these sources. Thus, it may also be the case that the H$^{13}CO^+$ emission is sensitive to the outflows in these regions. A correlation is observed between the SiO luminosity and the HCO$^+$ column density, which suggests a preference for increased SiO emission towards sources with higher densities, as seen in the low-mass regime (Gibb et al. 2004). Furthermore, we find the SiO luminosity is correlated with the CO outflow velocity, again showing the association of SiO emission with high-velocity outflows as seen in previous works (e.g. Gibb et al. 2007).

4.3 SiO luminosity with source evolution

SiO emission was predominantly detected towards Class 0 sources in the low-mass regime (Gibb et al. 2004), suggesting a preference for SiO emission towards younger, denser sources with faster outflows. However, in the high-mass regime the evolutionary sequence and outflow properties are less constrained, and previous works have found the observed SiO luminosity and integrated intensity to both increase and decrease as a function of evolution (e.g. Klaassen et al. 2012; Sánchez-Monge et al. 2013; Leurini et al. 2014). In this work we aim to establish if an evolutionary trend, as seen in the low-mass regime, does transfer to the high-mass regime. With this in mind, we purposely selected a sample of massive star-forming regions from the RMS survey with a range of luminosity and evolutionary stage (categorized into two evolutionary stages in the RMS survey:

Table 6. Spearman's rank correlation statistics for source properties as a function of the SiO luminosity. The *p*-value represents the probability of a correlation arising by chance, *R* is the resultant correlation coefficient, and *N* is the number of sources in each sample and the linear fit for SiO luminosity relationship is also given for properties showing a correlation. The Spearman's rank probability of false correlation, the linear correlation coefficient and the resulting linear regression fit were derived using the ASURV package (Feigelson & Nelson 1985; Isobe, Feigelson & Nelson 1986; Lavalley, Isobe & Feigelson 1992) considering the 3σ upper limits only. The linear fits are for the $\log_{10}$ of the SiO luminosity and the $\log_{10}$ of the source properties (excluding the $H^{13}CO^+$ FWHM and ^{12}CO (3–2) linewidth). The $H^{13}CO^+$ FWHM is extracted from the dendrogram fits to the full source extent.

Correlation with L_{SiO}	N	p-value	R	Linear fit
L_* (L$_\odot$)	32	0.509	–	–
$H^{13}CO^+$ FWHM (km s^{-1})	30	≤ 0.003	0.66	$\text{Log}_{10}(L_{SiO}) = (0.91 \pm 0.18) \times H^{13}CO^+ \text{ FWHM} - 0.58$
$C^{18}O$ FWHM (km s^{-1})	23	0.121	–	–
$L_{70\,\mu m}$ (L$_\odot$)	29	0.049	–	–
Mass (M$_\odot$)	23	0.033	–	–
N_{HCO+} peak (cm^{-2})	30	0.003	0.59	$\text{Log}_{10}(L_{SiO}) = (1.49 \pm 0.38) \times \text{Log}_{10}(N_{HCO+}) - 18.89$
N_{HCO+} average (cm^{-2})	30	0.003	0.64	$\text{Log}_{10}(L_{SiO}) = (2.63 \pm 0.62) \times \text{Log}_{10}(N_{HCO+}) - 34.05$
^{12}CO linewidth(km s^{-1})	23	≤ 0.004	0.62	$\text{Log}_{10}(L_{SiO}) = (0.04 \pm 0.01) \times {}^{12}CO \text{ linewidth} + 0.44$
M_{total} (M$_\odot$)	23	0.54	–	–
P_{total}(M$_\odot$km s^{-1})	23	0.08	–	–
E_{total} (ergs)	23	0.02	–	–
$\dot{M}_{total}$ (M$_\odot$yr^{-1})	23	0.11	–	–
$\dot{P}_{total}$ (M$_\odot$kms^{-1}yr^{-1})	23	0.01	0.60	$\text{Log}_{10}(L_{SiO}) = (1.18 \pm 0.32) \times \text{Log}_{10}(\dot{P}_{total}) + 5.14$
$\dot{E}_{total}$(L$_\odot$)	23	0.004	0.67	$\text{Log}_{10}(L_{SiO}) = (1.00 \pm 0.25) \times \text{Log}_{10}(\dot{E}_{total}) + 2.02$

massive YSOs (MYSOs) and compact H II regions; see Lumsden et al. 2013). A KS test shows no significant difference in the SiO luminosity between the MYSOs and H II regions. Moreover, the SiO luminosities of the OFFSET and H II/YSO sources also show no obvious differences compared with the MYSO sample.

4.3.1 Evolutionary indicators

We adopt the approach used by Sánchez-Monge et al. (2013) and López-Sepulcre et al. (2011) and compare the bolometric luminosity-to-mass ratio ($L_{bol}/M_\odot$), suggested as an indicator of the age of a given source, to the SiO luminosity in Fig. 4. Molinari et al. (2008) showed that as a source evolves the luminosity is expected to increase more rapidly than the core envelope mass, which is expected to decrease only slightly due to mass loss from winds and jets. An increase in the bolometric luminosity-to-mass ratio would potentially indicate a more advanced evolutionary stage. We find that all of the SiO non-detected sources have higher (>50 L$_\odot$/M$_\odot$) bolometric-to-luminosity ratios. The result of the KS test returns a *p*-value of 0.009 between the SiO-detected and SiO non-detected samples, suggesting they are drawn from different populations. However, it should be noted that the sample size for the non-detected sources is low and includes three of those sources without either an SiO detection or an associated CO outflow. As with the bolometric luminosity, we find no difference between the RMS classifications. This was previously observed by both Urquhart et al. (2014) and Maud et al. (2015a), where no indistinguishable differences in the bolometric luminosity-to-mass ratios between the MYSOs and compact H II regions from the RMS survey were found. This suggests that these sources are either likely to be at a similar evolutionary stage or it may be the case that the luminosity for this IR-bright stage has stopped rapidly increasing and the bolometric luminosity-to-mass ratio may not be sensitive enough to distinguish the evolutionary stages in this sample. For the offset source G203.3166-OFFSET or CMM-3[4] this source shows

the smallest bolometric luminosity-to-mass ratio in the sample, in agreement with it being a young protostar (e.g. Watanabe et al. 2015; Cunningham et al. 2016).

In addition, we use the ratio of mid- to far-IR colours as a potential indication of age in these sources. In Fig. 5 we plot the ratio of the 70 μm flux estimated from the *Herschel* data with the 22 μm WISE flux (F70/F22).[5] As a source evolves and the emission moves to shorter wavelengths, we would expect the F70/F22 colour ratio to decrease. A Spearman's rank correlation test gives a correlation coefficient of 0.76 and probability of a false correlation given by <0.001 between the SiO luminosity and the F70/F22 colour ratio. Thus, the SiO luminosity is stronger in the redder, potentially younger, more embedded sources. This may indicate that the colour ratio is more sensitive to evolution in these sources. However, a KS test between the SiO-detected and SiO non-detected sources only gives a *p*-value of $\sim$0.06 and is therefore not significant between the populations, which may again be a result of these sources being at a similar evolutionary stage. Csengeri et al. (2016) noted that the bolometric luminosity-to-mass ratio can be dominated by the most massive IR-bright source in the region; the F70/F22 colour ratio is also likely to suffer from this. Furthermore, as suggested by Maud et al. (2015b) there is evidence that several of these regions are likely to host multiple outflows at this spatial resolution (e.g. G081.7220/DR21 OH; Girart et al. 2013, CMM-3 in NGC2264-C; Watanabe et al. 2017). Additionally, we are assuming that the SiO emission is associated with the IR-bright RMS source in all regions, which was not the case towards G203.3166/NGC2264-C (Cunningham et al. 2016). This is likely to add scatter to the statistics.

5 CONCLUSIONS

We present the results of JCMT SiO (8–7), $H^{13}CO^+$, and HCO$^+$(4–3) survey towards a distance-limited sample of 31 massive star-forming regions drawn from the RMS survey. The presence of a

---

[4] The bolometric luminosity for this source is taken from Cunningham et al. (2016) and the mass is taken from the SCUBA mass estimated here.

[5] The WISE point source flux, extracted directly from the RMS survey data base, is used for the 22 μm flux. For one source, G012.9090, which does not have a *WISE* flux, the MSX 21 μm flux is used.
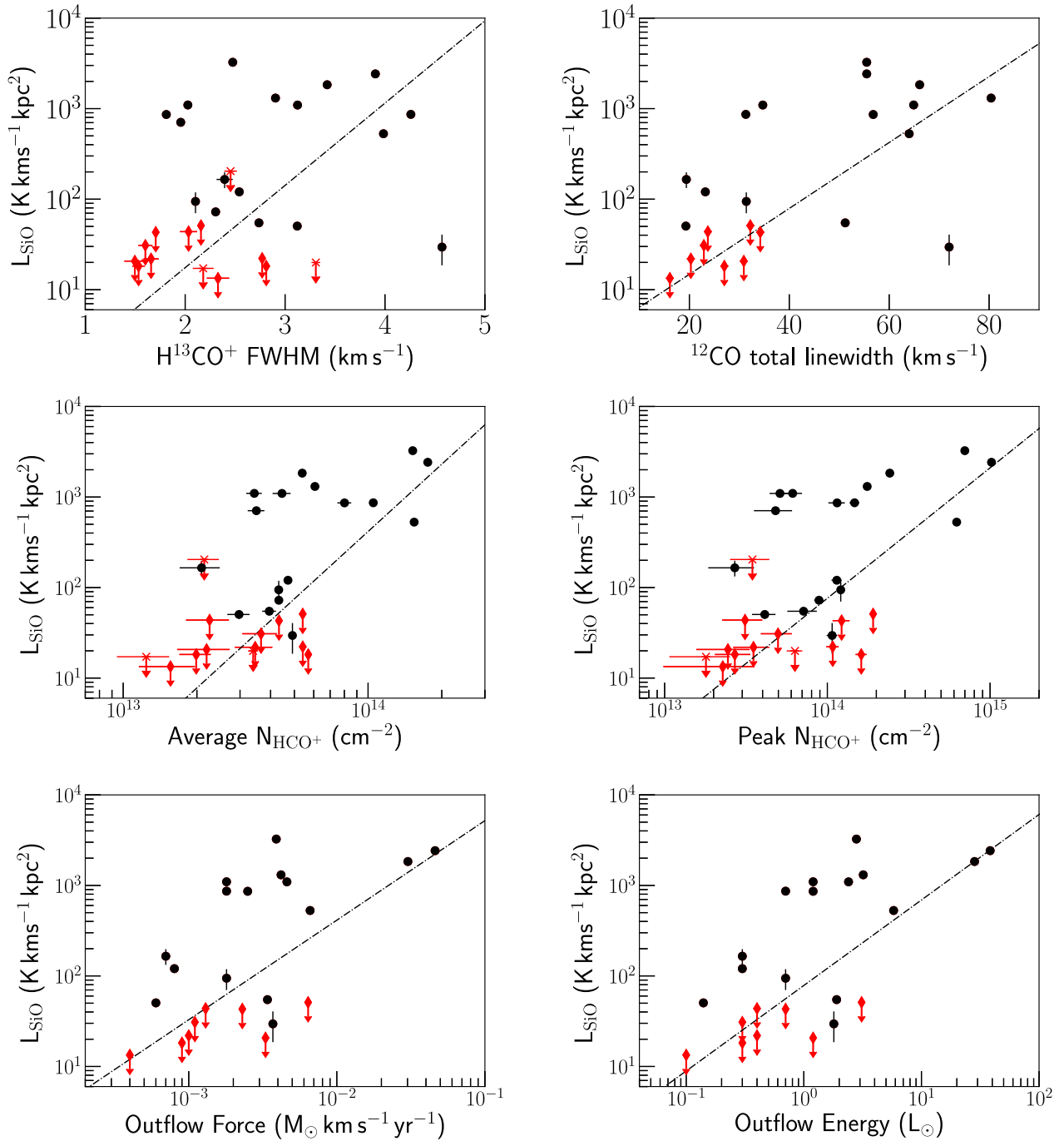
Figure 3. SiO luminosity as a function of source properties, for those parameter relationships given in Table 6 with a *p*-value ≤0.01 and a correlation coefficient >0.53. The plots include the $H^{13}CO^+$ FWHM, $^{12}CO\,(3–2)$ total linewidth or outflow velocity, average and peak HCO^+ column density, outflow force, and outflow energy. The black circles represent those sources with an SiO detection above 3σ that have a confirmed CO outflow detection in Maud et al. (2015b). The red diamonds and red crosses represent the 3σ upper limits for non-detected SiO sources with and without a CO outflow, respectively. The black dashed lines are linear regression fits (provided in Table 6) to the data. For sources that show no L_{SiO} error bars the errors are smaller than the symbols. It should be noted that the errors in the SiO luminosity do not account for uncertainties in source distance, and should be seen as minimal errors.

young, active outflow is associated with the detection of SiO (8–7) emission and we use previous $^{12}CO\,(3–2)$ data (Maud et al. 2015b) to determine outflow properties and identify potential fossil outflows. We explore the presence of possible global infall from the HCO^+ and $H^{13}CO^+\,(4–3)$ emission. Our results are summarized below.

(i) We detect SiO (8–7) emission towards ∼46 per cent of the sources, where the lack of an SiO detection does not appear to be due to sensitivity limitations or distance to the sources. We find only the CO outflow velocity shows a significant difference between SiO-detected (i.e. a potentially active outflow) and SiO non-detected (i.e. a potentially fossil remnant-driven outflow) sources. Thus, the
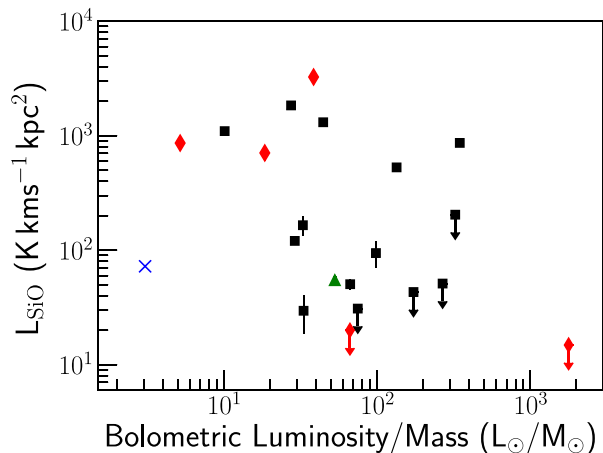
Figure 4. SiO luminosity as a function of bolometric luminosity-to-mass ratio ($L_\odot/M_\odot$). The black squares, red diamonds, and green triangle represent YSOs, H II, and H II/YSO sources with an SiO detection, respectively. Sources without an SiO detection are represented as upper limits using the same colours/symbols as for the SiO-detected sources. The blue cross represents the offset source G203.3166-OFFSET, where the bolometric luminosity estimate is taken from Cunningham et al. (2016). We do not have bolometric luminosity estimates for the remaining OFFSET sources, and, as such, are subsequently missing from the figure.
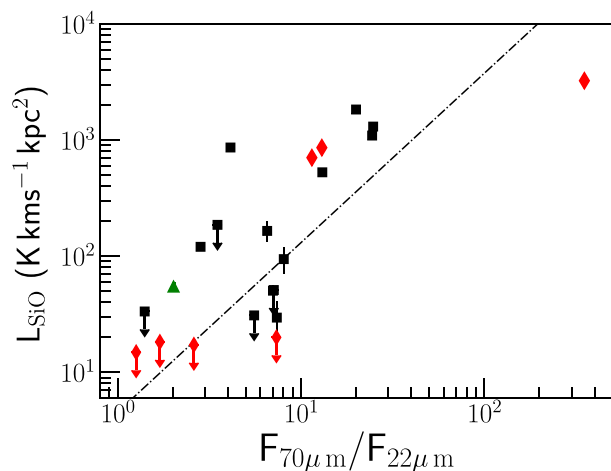

Figure 5. SiO luminosity as a function of the F70/F22 colour ratio. The symbols and colours are the same as in Fig. 4. The offset sources are not included as their 22 μm fluxes were not available. The linear fit is shown by the black dashed line and has a correlation coefficient of $R=0.76$ and a linear fit given by $\mathrm{Log}_{10}(L_{SiO}) = (1.46 \pm 0.30) \times \mathrm{Log}_{10}(F70/F22) + 0.66$.

detection of SiO is an indication of the presence of a high-velocity, likely active outflow and is consistent with the expected shock velocities required to disrupt dust grains. In addition, correlations between the SiO luminosity and the $H^{13}CO^+$ FWHM, HCO^+ column density, $^{12}CO\,(3–2)$ total outflow velocity, outflow force, and energy are found. Thus, the production and strength of the SiO emission are increased towards potentially more turbulent regions with increased column densities. Similarly, regions with faster and more powerful outflows are more likely to produce stronger SiO emission, as observed in the low-mass regime. However, it is possible the $H^{13}CO^+$ is also tracing the outflow emission in these sources.

(ii) We find tentative evidence from the bolometric-luminosity-to-mass ratio and F70/F22 colour ratios that sources with an SiO detection are associated with potentially younger, more embedded

regions. However, if multiple outflows are present or the SiO emission is not associated with the RMS source, this would likely add scatter to the statistics. Higher resolution observations are required to fully explore this.

(iii) We do not find a significant number of blue asymmetric profiles, indicative of global infall, towards these sources. However, $HCO^+(4–3)$ may not be best suited tracer, at this spatial resolution, to detect global infall signatures in these sources. Higher spatial resolution observations, where infall motions on to individual protostars can be resolved, will be able to directly probe this.

REFERENCES

Asaki Y., Imai H., Sobolev A. M., Parfenov S. Y., 2014, ApJ, 787, 54
Bally J., Reipurth B., Lada C. J., Billawala Y., 1999, AJ, 117, 410
Bonnell I. A., Bate M. R., Clarke C. J., Pringle J. E., 2001, MNRAS, 323, 785
Bontemps S., Andre P., Terebey S., Cabrit S., 1996, A&A, 311, 858
Buckle J. V. et al., 2009, MNRAS, 399, 1026
Csengeri T. et al., 2016, A&A, 586, A149
Cunningham N., 2015, PhD thesis, University of Leeds
Cunningham N., Lumsden S. L., Cyganowski C. J., Maud L. T., Purcell C., 2016, MNRAS, 458, 1742
Di Francesco J., Johnstone D., Kirk H., MacKenzie T., Ledwosinska E., 2008, ApJS, 175, 277
Duarte-Cabral A., Bontemps S., Motte F., Gusdorf A., Csengeri T., Schneider N., Louvet F., 2014, A&A, 570, A1
Feigelson E. D., Nelson P. I., 1985, ApJ, 293, 192
Flower D. R., Pineau des Forêts G., 2012, MNRAS, 421, 2786
Gibb A. G., Richer J. S., Chandler C. J., Davis C. J., 2004, ApJ, 603, 198
Gibb A., Davis C., Moore T., 2007, MNRAS, 382, 1213
Girart J. M., Frau P., Zhang Q., Koch P. M., Qiu K., Tang Y.-W., Lai S.-P., Ho P. T. P., 2013, ApJ, 772, 69
Guillet V., Jones A. P., Pineau Des Forêts G., 2009, A&A, 497, 145
Gusdorf A., Cabrit S., Flower D. R., Pineau Des Forêts G., 2008, A&A, 482, 809
Isobe T., Feigelson E. D., Nelson P. I., 1986, ApJ, 306, 490
Jenness T., Currie M. J., Tilanus R. P. J., Cavanagh B., Berry D. S., Leech J., Rizzi L., 2015, MNRAS, 453, 73
Klaassen P. D., Wilson C. D., 2007, ApJ, 663, 1092
Klaassen P., Testi L., Beuther H., 2012, A&A, 538, A140
Kutner M. L., Ulich B. L., 1981, ApJ, 250, 341
Larson R. B., 1981, MNRAS, 194, 809
Lavalley M., Isobe T., Feigelson E., 1992, in Worrall D. M., Biemesderfer C., Barnes J., eds, ASP Conf. Ser. Vol. 25, Astronomical Data Analysis Software and Systems I. Astron. Soc. Pac., San Francisco, p. 245
Leurini S., Codella C., López-Sepulcre A., Gusdorf A., Csengeri T., Anderl S., 2014, A&A, 570, A49
López-Sepulcre A. et al., 2011, A&A, 526, L2
Lu X., Zhang Q., Liu H. B., Wang J., Gu Q., 2014, ApJ, 790, 84

Lumsden S. L., Hoare M. G., Urquhart J. S., Oudmaijer R. D., Davies B., Mottram J. C., Cooper H. D. B., Moore T. J. T., 2013, ApJS, 208, 11

McKee C., Tan J., 2003, ApJ, 585, 850

Mardones D., Myers P. C., Tafalla M., Wilner D. J., Bachiller R., Garay G., 1997, ApJ, 489, 719

Maud L. T., Lumsden S. L., Moore T. J. T., Mottram J. C., Urquhart J. S., Cicchini A., 2015a, MNRAS, 452, 637

Maud L. T., Moore T. J. T., Lumsden S. L., Mottram J. C., Urquhart J. S., Hoare M. G., 2015b, MNRAS, 453, 645

Minh Y. C., Su Y.-N., Chen H.-R., Liu S.-Y., Yan C.-H., Kim S.-J., 2010, ApJ, 723, 1231

Molinari S., Pezzuto S., Cesaroni R., Brand J., Faustini F., Testi L., 2008, A&A, 481, 345

Molinari S. et al., 2010, A&A, 518, L100

Motte F., Bontemps S., Schilke P., Schneider N., Menten K. M., Broguière D., 2007, A&A, 476, 1243

Motte F. et al., 2010, A&A, 518, L77

Motte F., Bontemps S., Louvet F., 2017, preprint (arXiv:1706.00118)

Mottram J. C. et al., 2017, A&A, 600, A99

Myers P. C., Mardones D., Tafalla M., Williams J. P., Wilner D. J., 1996, ApJ, 465, L133

Peretto N. et al., 2014, A&A, 561, A83

Pilbratt G. L. et al., 2010, A&A, 518, L1

Poglitsch A., Waelkens C., Geis N., Feuchtgruber H., Vandenbussche B., Rodriguez L., Krause O., Renotte E., 2010, A&A, 518, L2

Rygl K. L. J., Wyrowski F., Schuller F., Menten K. M., 2013, A&A, 549, A5

Sánchez-Monge Á., López-Sepulcre A., Cesaroni R., Walmsley C. M., Codella C., Beltrán M. T., Pestalozzi M., Molinari S., 2013, A&A, 557, A94

Schilke P., Walmsley C. M., Pineau des Forets G., Flower D. R., 1997, A&A, 321, 293

Schneider N., Csengeri T., Bontemps S., Motte F., Simon R., Hennebelle P., Federrath C., Klessen R., 2010, A&A, 520, A49

Smith R. J., Shetty R., Beuther H., Klessen R. S., Bonnell I. A., 2013, ApJ, 771, 24

Tigé J. et al., 2017, A&A, 602, A77

Urquhart J. S. et al., 2014, MNRAS, 443, 1555

Walker-Smith S. L., Richer J. S., Buckle J. V., Hatchell J., Drabek-Maunder E., 2014, MNRAS, 440, 3568

Watanabe Y. et al., 2015, ApJ, 809, 162

Watanabe Y., Sakai N., López-Sepulcre A., Sakai T., Hirota T., Liu S.-Y., Su Y.-N., Yamamoto S., 2017, ApJ, 847, 108

Williams G. M., Peretto N., Avison A., Duarte-Cabral A., Fuller G. A., 2018, A&A, accepted (arXiv:1801.07253)

Wu Y. W. et al., 2014, A&A, 566, A17

SUPPORTING INFORMATION

Supplementary data are available at *MNRAS* online.

Appendix B. HCO^+, $H^{13}CO^+$ and SiO emission maps.

Please note: Oxford University Press is not responsible for the content or functionality of any supporting materials supplied by the authors. Any queries (other than missing material) should be directed to the corresponding author for the article.

APPENDIX A: $H^{13}CO^+$ GAUSSIAN FITS

Presented below are the resulting Gaussian fits to the $H^{13}CO^+$ spectra.

Table A1. Fitted parameters from a single Gaussian fit to the sum of the $H^{13}CO^+$ (4–3) line emission extracted from all pixels within $H^{13}CO^+$ (4–3) 5σ masked regions. Column 1 is the RMS name; Column 2 is the RMS classification; and Column 3 gives the total number of pixels in the $H^{13}CO^+$ (4–3) masks used to extract the emission. Columns 4, 5, 6, and 7 give peak, central velocity, FWHM, and integrated intensity from a single Gaussian fit to the sum of the $H^{13}CO^+$ (4–3) emission extracted from all pixels within the masked region.

Source name	Type	No of pixels	Summed T_{mb} (K)	V_{LSR} (km s^{-1})	δV (km s^{-1})	Summed $T_{mb}dv$ (K km s^{-1})
CO outflow						
G010.8411−02.5919	YSO	17	14.38 ± 0.76	11.98 ± 0.04	1.71 ± 0.10	26.12 ± 2.11
G012.9090−00.2607	YSO	38	19.94 ± 0.58	37.32 ± 0.05	3.42 ± 0.11	72.65 ± 3.21
G013.6562−00.5997	YSO	4	1.90 ± 0.12	48.00 ± 0.10	3.13 ± 0.23	6.32 ± 0.62
G017.6380+00.1566	YSO	33	27.57 ± 0.77	22.33 ± 0.03	2.16 ± 0.07	63.38 ± 2.71
G018.3412+01.7681	YSO	21	14.37 ± 0.56	32.84 ± 0.04	2.10 ± 0.10	32.19 ± 1.91
G043.3061−00.2106	H II	6	2.92 ± 0.21	59.28 ± 0.08	2.40 ± 0.20	7.45 ± 0.81
G045.0711+00.1325	H II	13	6.97 ± 0.14	59.10 ± 0.06	6.20 ± 0.15	45.98 ± 1.43
G050.2213−00.6063	YSO	4	0.96 ± 0.15	40.36 ± 0.23	2.90 ± 0.54	2.97 ± 0.72
G078.1224+03.6320	YSO	22	14.26 ± 0.46	− 3.32 ± 0.05	3.12 ± 0.12	47.39 ± 2.35
G079.1272+02.2782	YSO	5	2.74 ± 0.26	− 1.58 ± 0.09	1.81 ± 0.20	5.28 ± 0.77
G079.8749+01.1821	H II	5	2.16 ± 0.29	− 4.90 ± 0.10	1.54 ± 0.24	3.53 ± 0.71
G079.8749+01.1821-OFFSET	–	19	12.84 ± 0.49	− 3.14 ± 0.05	2.81 ± 0.12	38.44 ± 2.25
G081.7133+00.5589	YSO	8	8.63 ± 0.53	− 4.09 ± 0.08	2.47 ± 0.18	22.76 ± 2.14
G081.7220+00.5699	H II	53	58.83 ± 1.32	− 3.17 ± 0.05	4.57 ± 0.12	286.36 ± 9.84
G081.7522+00.5906	YSO	23	18.58 ± 0.70	− 4.04 ± 0.04	2.03 ± 0.09	40.11 ± 2.29
G081.7522+00.5906-OFFSET	–	20	13.02 ± 0.51	− 3.19 ± 0.05	2.77 ± 0.12	38.43 ± 2.28
G081.7624+00.5916-OFFSET	YSO	19	11.11 ± 0.94	− 4.34 ± 0.08	1.96 ± 0.19	23.2 ± 3.03
G081.8652+00.7800	YSO	–	–	–	–	–
W75N	–	56	83.83 ± 0.75	9.67 ± 0.017	3.90 ± 0.04	348.53 ± 4.78
G081.8789+00.7822	H II	–	–	–	–	–
G083.0936+03.2724	H II	4	0.89 ± 0.22	− 3.50 ± 0.29	2.33 ± 0.67	2.22 ± 0.84
G083.7071+03.2817	YSO	–	–	–	–	–
G083.7071+03.2817-OFFSET	–	4	1.95 ± 0.35	− 3.62 ± 0.13	1.50 ± 0.31	3.11 ± 0.85
G083.7962+03.3058	H II	4	2.78 ± 0.33	− 4.31 ± 0.10	1.66 ± 0.23	4.91 ± 0.88
G103.8744+01.8558	YSO	5	3.80 ± 0.55	− 18.30 ± 0.11	1.60 ± 0.27	6.49 ± 1.44
G109.8715+02.1156	YSO	71	91.63 ± 1.31	− 10.80 ± 0.03	3.99 ± 0.07	388.87 ± 8.49
G192.6005−00.0479	YSO	5	4.11 ± 0.14	7.84 ± 0.07	4.26 ± 0.17	18.65 ± 0.98
G194.9349−01.2224	YSO	4	1.48 ± 0.27	15.61 ± 0.18	2.03 ± 0.43	3.20 ± 0.89
G203.3166+02.0564	YSO	50	34.05 ± 1.06	8.15 ± 0.04	2.31 ± 0.08	83.60 ± 3.96
G203.3166+02.0564-OFFSET	–	28	15.87 ± 0.56	7.55 ± 0.04	2.54 ± 0.10	42.96 ± 2.32
G207.2654−01.8080	H II/YSO	12	5.77 ± 0.45	12.58 ± 0.10	2.74 ± 0.24	16.83 ± 1.98
No CO Outflow						
G080.8645+00.4197	H II	11	3.76 ± 0.22	− 2.75 ± 0.095	3.31 ± 0.22	13.26 ± 1.17
G080.9383−00.1268	H II	–	–	–	–	–
G081.7131+00.5792	YSO	–	–	–	–	–
G196.4542−01.6777	YSO	4	1.16 ± 0.18	19.34 ± 0.18	2.46 ± 0.43	3.20 ± 0.89
G217.3771−00.0828	H II	4	0.76 ± 0.17	23.93 ± 0.25	2.18 ± 0.58	1.76 ± 0.62
G233.8306−00.1803	YSO	–	–	–	–	–

This paper has been typeset from a TEX/LATEX file prepared by the author.